HHS Public Access

Author manuscript

*Magn Reson Med*. Author manuscript; available in PMC 2017 April 01.

Published in final edited form as:

*Magn Reson Med*. 2016 April ; 75(4): 1685–1696. doi:10.1002/mrm.25725.

# Longitudinal Assessment of Spinal Cord Injuries in Non-human Primates with Quantitative Magnetization Transfer

**Feng Wang**[1,2], **Ke Li**[1,2], **Arabinda Mishra**[1,2], **Daniel Gochberg**[1,2], **Li Min Chen**[1,2,4,*], and **John C. Gore**[1,2,3,4]

[1] Institute of Imaging Science, Vanderbilt University, Nashville, TN 37232

[2] Radiology and Radiological Sciences, Vanderbilt University, Nashville, TN 37232

[3] Biomedical Engineering, Vanderbilt University, Nashville, TN 37232

[4] Psychology, Vanderbilt University, Nashville, TN 37232

## Abstract

**Purpose—**This study aimed to evaluate the reproducibility and specificity of quantitative magnetization transfer (qMT) imaging for monitoring spinal cord injuries (SCIs).

**Methods—**MRI scans were performed in anesthetized monkeys at 9.4T, before and serially after a unilateral lesion of the cervical spinal cord. A two-pool fitting model was used to derive qMT parameters.

**Results—**qMT measures were reproducible across normal subjects, with an average pool size ratio (PSR) of 0.086 ± 0.003 (Mean ± SD) for gray matter, and 0.120 ± 0.005 for white matter, respectively. Compared to normal gray matter, the PSR of abnormal tissues rostral and caudal to the injury site decreased by 19.5% ($p < 0.05$), while the PSR of the cyst-like volume decreased drastically weeks after SCI. Strong correlations in cyst-like regions were observed between PSR and other MRI measures including longitudinal relaxation rate ($R_1$), apparent diffusion coefficient (ADC) and fractional anisotropy (FA). Decreased PSR and FA values correlated well with demyelination in abnormal tissues.

**Conclusion—**The qMT parameters provide robust and specific information about the molecular and cellular changes produced by SCI. PSR detected demyelination and loss of macromolecules in abnormal tissue regions rostral and caudal to the cyst/lesion sites.

### Keywords

MRI; quantitative magnetization transfer (qMT); demyelination; spinal cord injury; cyst; 9.4T

[*] Corresponding author Li Min Chen, MD, PhD, Associate Professor, Department of Radiology and Radiological Sciences Institute of Imaging Science AA 1105 MCN 1161 21st Ave. S. Nashville, TN, 37232 Tel: (615) 9367069 Fax: (615) 3220734 limin.chen@vanderbilt.edu.

SUPPORTING INFORMATION

**A**dditional supporting information may be found in the online version of this article.

## INTRODUCTION

Injury may disrupt the normal functions of the spinal cord (SC), and lead to severe sensory and motor behavioral deficits. Over time, the impaired functions may recover through different mechanisms at both the SC and brain levels (1-3). Regeneration of injured SC is a key process during functional recovery, and has been a major topic of research for developing improved therapies. Spinal cord injury (SCI) can induce cell death and create tissue cavities, while subsequent reactions including inflammation can stimulate both destructive and reparative processes (3), and lead to edema and cysts (2) and demyelination (4,5). SCI also culminates in glial scarring, and the scar tissue may contain secreted and transmembrane molecular inhibitors of axon growth (6,7). To be able to evaluate potential new treatments, it is important to understand the temporal changes and recovery of injured SC tissue from structural, functional and molecular perspectives. Non-invasive quantitative magnetic resonance imaging (MRI) methods are well suited for monitoring the recovery process in a comprehensive way. Furthermore, validation of MRI measures of compositional and structural changes that occur at and around spinal lesion sites is crucial for the interpretation of MRI findings. A model of SCI in monkeys provides a valuable experimental platform for these purposes.

Quantitative MRI studies of the SC (8-12) have been challenging, partly due to the technical challenges related to the small size of SC, and the presence of cerebral spinal fluid (CSF) pulsation associated with cardiac and respiratory cycles. To date, a variety of quantitative MRI methods (13,14) are available for the study of injured SC (12,15-26) and its recovery in behaving animals (27,28), which are also translatable to human SCI patients (28,29). The uniqueness and power of such an approach have been well demonstrated in our previous study in monkeys using multi-parametric MRI (12). As an extension of that first study, here we report our longitudinal investigation of SCI using quantitative magnetization transfer (qMT) imaging to derive additional information on tissue compositional changes.

Magnetization transfer (MT) is the spin exchange between proton pools in different environments, and can be used to evaluate macromolecular content of tissue (30,31). There are two main approaches to measure MT effects: semi-quantitative magnetization transfer ratio (MTR) and qMT methods that extract numerical parameters based on a specific model. To date, simpler metrics such as MTR (32) have been the major approach to assess changes in macromolecular composition in neurological disorders (33,34), neuromuscular diseases (35), liver fibrosis (36), and cancer (37). MTR has also been shown to be sensitive to changes in protein content and has been used previously in studies of SC (12,38,39). The sensitivity and reproducibility of MTR measure can be influenced by various experimental parameters. To increase specificity and sensitivity, qMT methods have been developed to measure intrinsic MT parameters, and to isolate the pool size ratio (PSR, the ratio of the macromolecular proton pool to the free water pool) from relaxation rates and exchange rates (40-42).

In this study we employed a pulsed saturation qMT data acquisition and the simplified Henkelman-Ramani model (43,44) for studying the SC of squirrel monkeys. Multiple qMT parameters, including PSR, transverse relaxation rates $R_{2a}$ and $R_{2b}$, and exchange rate

$RM_{0b}$, were derived from the model fitting, and the observed spin-lattice relaxation rate $R_{1obs}$ was measured separately. We correlated the PSR with other qMT, diffusion tensor imaging (DTI) and chemical exchange saturation transfer (CEST) measures of changes in tissue properties after SCI. All qMT parameters exhibited good cross-subject reproducibility and were sensitive for detecting the tissue composition changes following injury.

## METHODS

### Animal preparation

Nine male squirrel monkeys (*Saimiri sciureus*, 6-8 years old) were included in this study. Three of them, identified as SM-G, SM-P and SM-T, underwent a unilateral dorsal column transection between cervical 4-5 levels (C4-C5). Lesioned subjects were scanned before, and at different time points after injury (e.g. 2, 3, 6, 7, 8, 10, 12, 14, 16 or 24 weeks). The behavioral deficits of SM-G and SM-P were severe and SM-T was moderate (for behavioral assessment criteria see details in supporting information). During MRI scans, each monkey was anesthetized (isoflurane 0.5-1.5%) and mechanically ventilated, with head and body stabilized in an MR compatible frame. Vital signs including heart rate, core body temperature, end tidal $CO_2$, and $SpO_2$ were monitored and maintained throughout the entire imaging session. All procedures were approved by the IACUC (Institutional Animal Care and Use Committee) of Vanderbilt University.

### In vivo MRI

All MR images were acquired on a 9.4T Agilent MRI scanner using a saddle-shaped transmit-receive surface coil positioned around the cervical spine region. The image field of view was centered at C4 level, where the lesion was targeted. High resolution magnetization transfer contrast (MTC) images (in plane resolution of $0.313 \times 0.313$ $mm^2$) were acquired using a gradient echo sequence (TR/TE=220/3.24 ms, matrix size=128×128), which incorporated a Gaussian saturation pulse at RF offset of 5000 Hz and flip angle 820°. Ten slices were acquired from orthogonal imaging planes, and the thickness was 0.5 mm for coronal, 0.75 mm for sagittal, and 2 mm for axial slices.

Quantitative MT data were obtained for one single coronal slice placed at the posterior portion of the SC where the dorsal columns and dorsal horns reside (Fig. 1a-b). To ensure that the same region was sampled for quantitative comparisons across imaging sessions, we used local fiducial landmarks on high-resolution sagittal and axial MTC images to place the single coronal slice. Those landmarks included the cervical nerve bundles (which indicate which segments were sampled), and the gray-white matter butterfly-shaped structure on the axial images. The coronal slice was placed at 0.5 mm from the posterior outer edge of white matter (WM) at the level of the lesion (C4). The first test data set was collected using a 2D MT-weighted spoiled gradient recalled-echo sequence (TR 24 ms, flip angle =7°, 48 acquisitions). Slice-selective Gaussian-shaped saturation pulses (flip angles = 220° and 820°, pulse width = 12 ms) were used, with 18 different RF offsets ranged between 100 Hz and 100 kHz with a constant logrithmic interval (Fig. 1c). Signals acquired with RF offsets smaller than 500 Hz showed drastic drops in amplitude (Fig. 1c-d), and we excluded those data points from later data acquisitions as suggested in previous publications (43,44).

Previous qMT imaging of human brain has suggested the minimal number of RF sample points (43-45). However, in the spinal cord the motion artifacts could strongly impact the accuracy of estimating (using pixel-by-pixel fitting) qMT parameters, if only sparse numbers of RF offsets are used. Thus, we acquired 12 different RF offsets, ranged between 800 Hz and 80 kHz with a constant logarithmic interval, at 2 saturation powers (which required 40 minutes of imaging time) to ensure an accurate modeling and derivation of qMT parameters. Observed relaxation rate $R_{1obs}$ and $B_1$ maps were obtained based on images acquired with two flip angles, whereas data for $B_0$ mapping were calculated from two gradient echo images (ΔTE = 2 ms). CEST and DTI data were acquired within the same imaging session, and the specific data acqusition and analysis methods are described in the supporting information as well as in our previous report (12).

## Data Analysis

Data obtained from the pre-lesion condition in three lesioned animals and six other normal animals were included in the group qMT quantification. All MRI data were analyzed using MATLAB 2011a (The Mathworks). All intra-session images used in quantification were coregistered using a rigid registration algorithm based on mutual information (46). The $B_1$ map was calculated using the saturated double angle method, $B_0$ map was calculated using a two-point Dixon method, and $T_{1obs}$ was obtained using the dual-angle approach (8).

Figure 1d shows the fitting of the model to normalized signals obtained from a selected voxel of regular gray matter (GM) in SC at different MT saturation powers ($\theta_{sat}$ = 220° and 820°) and frequency offsets. Henkelman-Ramani's model was applied to derive qMT parameters (43,44).

$$SI(\omega_1,\Delta f) = \frac{M_0\left(R_b\left[\frac{RM_{ob}}{R_a}\right]+R_{RFB}(\omega_{1CWPE},\Delta f,T_{2b})+R_b+\frac{RM_{0b}}{F}\right)}{\left[\frac{RM_{0b}}{R_a}\right](R_b+R_{RFB}(\omega_{1CWPE},\Delta f,T_{2b}))+\left(1+\left[\frac{\omega_{1CWPE}}{2\pi\Delta f}\right]^2\left[\frac{1}{T_{2a}R_a}\right]\right)\left(R_{RFB}(\omega_{1CWPE},\Delta f,T_{2b})+R_b+\frac{RM_{0b}}{F}\right)} \quad (1)$$

where ***a*** and ***b*** denote the free water pool and macromolecular pool, respectively. F is the relative size of the macromolecular pool, defined as $F=M_{0b}/M_{0a}$. $M_{0a}$ and $M_{0b}$ are the fully relaxed values of magnetization associated with the two pools, and $M_0$ is the signal without MT-weighting. The continuous wave power approximation (CWPE) was applied and $\omega_{1CWPE}$ is the amplitude of the saturating field (43,44). Δf represents the frequency offset of the MT pulse. $R_{RFB}$ is the rate of saturation of longitudinal magnetization in pool ***b*** due to the irradiation by the amplitude defined by $\omega_{1CWPE}$ and Δf (44), which is also dependent on the transverse relaxation time of the macromolecular pool $T_{2b}$. A super-Lorentzian line shape is used to represent the bound pool (44). R is the exchange rate constant. $R_a$ and $R_b$ are the respective longitudinal relaxation rates. Additional constraints were imposed to determine qMT parameters. $R_b$ was kept fixed at 1 $s^{-1}$ as usual (40,43,44). Another constraint was imposed by measuring the observed longitudinal relaxation rate $R_{1obs}$ independently, which was linked to $R_a$ (40).

$$R_a = R_{1obs} - RM_{0b}\,(R_b - R_{1obs}) \,/\, \left(R_b - R_{1obs} + \frac{RM_{0b}}{F}\right) \quad (2)$$

$M_0$, F, $RM_{0b}$, $T_{2a}$ and $T_{2b}$ were determined from the model fitting. The PSR was defined as the "F" value from the fitting. The fitting quality at each pixel was evaluated by the root mean squares (RMS) of the residuals at each RF offset. For data points with RF offsets smaller than 500 Hz, large residuals were observed between the model fitting results and raw data (Fig. 1d). The corresponding PSR and RMS maps overlaid on a high-resolution structural MTC image are shown in Figure 1e.

High-resolution MTC images were referenced for manual selection of ROIs (regions of interests) such as GM, WM and cyst for quantification (Fig. 2e). ROIs with homogeneous $B_0$ and $B_1$ were selected and included in the statistical analysis (<1.5 cm in length). To minimize partial volume effects, small ROIs were selected and voxels residing along the SC – CSF border were excluded. The abnormal tissue (AT) voxels were selected according to their low PSR values. The normal PSR range was defined as Mean ± 2SD (standard deviation, 95%) of the normal tissues on the non-lesion side, and AT was defined as voxels with PSR out of this normal range. Typically the AT region of interest was smaller than 3 mm in length, which corresponds to one spinal segment in this species. The significance of measurement differences was evaluated using Student's t-tests. The Pearson correlation coefficient ρ was calculated using the Pearson correlation function.

### Dorsal column section

In brief, under surgical level anesthesia and aseptic conditions, the dorsal portion of the low cervical spinal cord at C4-C6 level was exposed. The dorsal column was transected on one side with a pair of fine surgical scissors at the cervical level C4-C5. The lesion was 2 mm deep and ran from the middle line to the spinal nerve entering zone (~ 2 mm in width). The dura were replaced, and the opening was closed. The details of the surgical procedures can be found in previous publications (47,48).

### Histology

Histological stains of post-mortem tissue were used 1) to evaluate the level and extent of the spinal cord lesion, 2) to quantify the degree of afferent disruption of the dorsal column, and 3) to correlate with MRI measures. The complement of the myelin stain image was calculated. Then the degree of demyelination was assessed by the percent decrease of the averaged regional myelin stain intensity while the intensity of the corresponding region on the non-lesion side was used as a control (100%). More technical details are described in the supporting information.

## RESULTS

### QMT measures in normal spinal cord

In normal (or pre-lesion) spinal cord, with MT saturation, GM appeared to be brighter than WM, and a very thin layer of CSF around the spinal cord showed hyperintensity (Fig. 1c). In

the PSR map (Fig. 1e), WM showed larger values than GM. Regional analysis was employed and Table 1 summarizes the averaged qMT parameters of WM and GM across subjects. Except $T_{2a}$ and $RM_{0a}$, parameters PSR, $T_{2b}$ and $RM_{0b}$ were significantly different between GM and WM. These spinal qMT measurements were in similar range to those obtained in WM and GM of brain (43,44).

### MTC images revealed structural changes at the lesion and surrounding tissues

MTC images detected structural changes as early as post-lesion week 2. In subject SM-G, the lesions at a rostral C4 location occurred as a signal void, and an abnormal volume (AV), which later was determined to be a cyst, was also detected around the lesion site (Fig. 2b-d). The signal intensities of the cyst were relatively homogeneous, hyperintense to GM and isointense to CSF. The size of the cyst was about $2.0 \times 1.5 \times 2.3$ $mm^3$ in 7 weeks after lesion. The MT contrast allowed precise localization of spinal cord and selection of ROIs such as WM, GM and cyst for quantifications. Sample region of interest outlines are shown in Figure 2e.

### QMT detected PSR changes at the cyst and abnormal tissue regions

In all SCI subjects, PSR maps revealed lesion related changes (Fig. 3b&e), which were constrained to the lesion side. Compared to pre-injury PSR maps (left maps in Fig. 3b&e), post-lesion PSR maps identified a very low PSR region (a cyst, indicated by the red arrows in Fig. 3b&e), and two relatively low PSR regions on both rostral and caudal sides of the cyst (white arrows in Fig. 3b&e) in both GM and WM. These changes around the cyst were not evident on MTC images. Similar observations were present in both subjects (SM-P and SM-G), but the affected area sizes looked different depending on lesion level. The PSR of the signal void (SV) region, likely corresponding to the tissue cavity and associated hemorrhage caused by the lesion, could not be determined due to the low intensity in the raw images.

Normalized qMT spectra obtained with 2 different flip angles, with intensity at each point normalized to that at 80000 Hz, showed regional differences in both subjects (Fig. 3c&f). The normalized signals of GM were slightly higher than those of WM in the frequency offset range of 2000 to 10000 Hz. However, the normalized signals of the cyst were much higher (circles in Fig. 3c&f) than GM and WM at frequency offsets ranging from 800 to 10000 Hz. Consistent with the observations on PSR maps, abnormal tissue (AT) regions on both sides of the cyst showed signal enhancements (diamonds in Fig. 3c&f) compared to the GM on the non-lesion side of spinal cord.

### Intra-subject longitudinal assessment of the PSR after a spinal cord lesion

Serial MT imaging of the same subject revealed dynamic changes in structural features and the PSRs of different spinal cord ROIs after SCI. For example, a hyperintense cyst was detected in the dorsal column region on MTC images (Fig. 4a). At the trauma region outside the spinal cord and posterior to the lesion site, soft tissues also exhibited hyperintense MTC signals.

After SCI, the PSRs of the normal tissues on the non-lesion side appeared to be stable (Fig. 4b). The averaged PSR measures obtained across 6 longitudinal sessions before and after SCI were 0.121±0.004 and 0.084±0.003 for WM and GM respectively. In contrast, the PSRs of the cyst and abnormal tissue showed dynamic changes. The PSR in cyst was very low ($p<0.01$ vs. GM) at week 2, and remained low during the recovery. In contrast, the PSR in AT showed significant and continuous decreases from week 2 ($p<0.05$ vs. GM) to 10. Compared to normal GM, the degrees of PSR reduction were greater for the cyst (55.5% and 64.7%) than the AT (8.2% and 22.4%) (Fig. 4b). Similar trends of changes were observed in the other subjects.

### Longitudinal variations of MRI measures after a spinal cord lesion

We next compared the dynamic changes of qMT parameters PSR, $T_{2a}$, $T_{2b}$ and $RM_{0b}$, and other MRI measures including $T_{1obs}$, ADC, FA and amide proton transfer (APT*) in Figure 5 and Supporting Table. To simplify the comparison, we quantified each parameter at three time points after SCI: the onset point (OP, 2 weeks after SCI), peak point (PP, when the APT* of the cyst is at maximum, 3-10 weeks after SCI), and end point (EP, 14 weeks after SCI) after SCI.

Using normal GM as a control, the values of PSR, $T_{2b,}$ $RM_{0b}$ and FA in the cyst decreased whereas those of $T_{2a,}$ ADC, APT* and $T_{1obs}$ increased at OP, and then changed in opposite directions after they reached the minimum or maximum (Fig. 5). Among the qMT parameters, cyst showed more significant changes in PSR, $RM_{0b}$ and $T_{2a}$ ($p < 0.01$) than in $T_{2b}$ ($p < 0.05$) at the EP (Fig. 5 and Supporting Table). The ADC values of cyst were close to that of free water (~2.6 $\mu m^2$/ms) at PP, indicating a very low cell density. Over time, the ADC value decreased to ~1.9 $\mu m^2$/ms. $T_{1obs}$ and $T_{2a}$ of cyst were much larger than those of regular GM and WM at all the time points after SCI. APT* of cyst increased to the maximum from OP to PP (~20%), and then returned to baseline level from PP to EP. $T_{2a}$, APT*, ADC and FA characterized the further transient variations ($p<0.05$) in cyst after its onset (see # and $ in Fig. 5).

Compared to cyst, most parameters of AT changed less. PSR differentiated pathological changes ($p < 0.05$) from onset point (OP) to end point (EP) in AT, and it showed the highest sensitivity to AT at the EP ($p < 0.01$). APT* showed significant transient changes in AT from peak point (PP) to EP, but it did not show sensitivity at the EP. FA and $T_{2a}$ were also sensitive to AT ($p <0.05$). Pearson coefficient $\rho$ was calculated between time courses of PSR and other MRI parameters in both AT and cyst regions after injury (Supporting Table). Longitudinally, PSR correlated strongly with other parameters except APT* in the cyst. Only qMT measures of $T_{2b}$ and $RM_{0b}$ ($\rho > 0.95$) as well as FA ($\rho = 0.87$) correlated well with PSR in AT regions longitudinally. Compared to regular GM, the MRI parametric difference of cyst and AT at the EP indicates that full recovery was not completed at the lesion sites during the period of our study. In summary, all the measures were sensitive in detecting the cyst, and PSR showed highest sensitivity ($p < 0.01$) for detecting abnormal tissue property changes at the EP (Figs. 5a&g).

### Regional Correlations between PSR and other MRI parameters

To understand the relationships between other MRI parameters and PSR that most closely relate to demyelination and macromolecular composition, regional Pearson correlations were calculated in ROIs of WM, GM, AT and cyst (Fig. 6). Relaxation rates ($R_{2a}=1/T_{2a}$, $R_{2b}=1/T_{2b}$, and $R_{1obs}=1/T1_{obs}$) were plotted against PSR in Figure 6. Several features were noticeable. First, measures from each ROI clustered together (Fig. 6a-g). In addition to qMT parameters PSR, $R_{2b}$, and $RM_{0b}$, the conventional measure FA also showed significant contrast between normal WM (0.76 ± 0.04) and GM (0.45 ± 0.02). Second, measures from different ROIs were isolated, except for some overlap between GM and AT. The clusters of cysts were fully separated from clusters of tissues. Third, most parameters were roughly related to PSR in a linear relationship when PSR is larger than 0.06 (the range for tissues including AT, GM and WM), except for APT*. The APT* of cyst and AT showed scattered values off the APT*-PSR slope of normal WM and GM, presumably due to the transient high levels of metabolites and mobile proteins/peptide related to secondary damage or inflammation. The clusters of cysts were away from the linear slope of normal tissues. Either positive or negative regional correlations were present between the PSR and all other parameters (Fig. 6h). The PSR was positively correlated with parameters of $R_{1obs}$, $R_{2a}$, $RM_{0b}$ and FA, and was negatively correlated with $R_{2b}$, ADC and APT*. Among all the MRI parameters, the regional correlation between APT* and PSR was the smallest ($\rho= -0.565$). Comparing the two DTI parameters, the regional correlation between ADC and PSR ($\rho= -0.632$) is much weaker than that between FA and PSR ($\rho= 0.963$).

### Histological confirmation of MRI findings

We stained the post -mortem spinal cord tissue sections for myelin, Cholera Toxin B (CTB), and Glial Fibrillary Acidic Protein (GFAP) in order to evaluate changes in the spinal cord caused by injury for each animal. Using manually placed landmarks, all tissue sections (Fig. 7h-j) were aligned with the MRI maps at the EP (Fig. 7a-g). CTB stains confirmed the lesion was localized at the C4 level where the roots enter, as evidenced by the CTB terminal labels from finger injections (see the example labels in red box of Fig. 7i). The lesion site (SV, yellow asterisk in Fig. 7a-g) was filled with soft tissue (yellow asterisk in Figure 7j). The AT regions rostral and caudal to the cyst/lesion exhibited different myelin and GFAP staining (red arrows in Fig. 7h,j). The spatial territory of the demyelination observed in the myelin stain was in general agreement with the regions with low PSR (red arrows in Fig. 7g&h). The cyst was identified as a tissue cavity (Fig. 7h-j). GFAP stains confirmed the nature of cyst, which was surrounded by degenerated swollen axons (Fig. 7j). Swollen axonal sheaths and gliosis, and high density of reactivated glia cells were observed (12). Similar features have been reported previously in specimens from SCI patients (49).

### Comparison of PSR with other MRI maps

To evaluate the specificity of PSR for detecting changes in tissue properties, we further compared PSR map with $T_{1obs}$, FA, ADC, and APT* maps at the EP qualitatively (Fig. 7a-g). All maps except the APT* (Fig. 7d) clearly detected the cyst. However, only the FA and PSR maps detected the regional demyelination and tissue property changes in the white and gray matters rostral and caudal to the lesion/cyst (compare Fig. 7b&g with Fig. 7h).

Compared to the PSR map, the FA appeared to be affected more by residual motion and partial volume effects (black arrow in Fig. 7b).

To quantify the specificity of PSR for detecting demyelination, we correlated directly the PSR decreases with the optical intensity changes on the myelin stains at four regions of interest (ROIs), with four from the non-lesion side as controls (Fig. 7k). We found that the degree of demyelination (indicated by intensity decreases, red columns) in general was correlated with the decreases in PSR (black columns, Pearson correlation coefficient $\rho > 0.99$) and MTR with saturation flip angle at 220° (dark grey columns, $\rho = 0.966$), but to a less degree with MTR at 820° flip angle ($\rho = 0.887$) and FA ($\rho=0.696$). $R_{1obs}$, ADC and APT* only correlated weakly with the myelin stain intensity, with $\rho$ values of 0.397, 0.041 and -0.235 respectively. Across different ROIs, the greatest PSR decrease was observed in the WM on the rostral side of the lesion/cyst, where the demyelination was most severe (see supporting Figure). GM showed much smaller percent decreases in PSR values.

## DISCUSSION

### Reproducibility and Specificity of qMT parameters

Compared to conventional 2-point MTR measurements, the qMT parameters provide more accurate and stable indicators of the macromolecular composition of tissue (Fig. 7k). Because the measure of PSR is relatively independent of pulse sequence, field strength and acquisition parameters, it is more consistent and reproducible and can be directly compared across imaging sessions within the same or across subjects. We showed that all qMT parameters exhibited good sensitivity for monitoring cyst formations following SCI. Among the parameters, PSR showed the highest specificity and reliability for detecting demyelination and loss of macromolecules in abnormal tissue regions rostral and caudal to the cyst/lesion sites (Fig. 5). These observations are expected because the PSR is known to be a more accurate and reliable indicator of content of macromolecules such as myelin and other proteins (50). In contrast, $T_{2a}$, being a measure of transverse relaxation time of the free water pool, is good at detecting changes in the cyst. Exchange rates are highly associated with protein and water contents but at high field may also reflect changes in chemical exchange of water and labile protons. The significantly decreased PSR, increased $T_{2a,}$ decreased $T_{2b}$ and $RM_{0b}$ in the cyst demonstrate the sensitivity of the qMT measures for quantifying changes in tissue macromolecule level and free water content. Over time, the cyst and the demyelinated tissue underwent a shrinkage process, during which the water content decreased while the macromolecule level increased. In summary, indications derived from the different qMT measures appeared to be more specific than other MRI metrics to changes in water content, myelination, and macromolecule level in abnormal spinal cord tissue surrounding the injury.

### MRI parameters and their regional correlation in injured spinal cord

This multi-parametric MRI study showed regional correlations between PSR and other MRI measures related to SCI. In principle, different MRI parameters quantify different aspects of tissue abnormalities. PSR is an indirect marker of myelin content. Relaxation rates are highly correlated with concentrations of macromolecules such as proteins. $R_{2a}$ increases as

PSR increases, a positive correlation as expected when the macromolecular source of relaxation changes. The $R_{2a}$ of the cyst lies out of the linear range of tissues in the plot of $R_{2a}$ versus PSR; the solid contribution to PSR in cyst appears to have a higher relaxivity (indicated by the line slope) than the corresponding normal tissues suggesting they may affect $T_{2a}$ of water by additional or more efficient mechanisms such as chemical exchange. The $R_{1obs}$ measured for cyst can be related to myelin content and formation of cyst, and this explains the strong positive correlation observed between $R_{1obs}$ and PSR. The ADC value reflects the diffusivity of water along and perpendicular to axons within the tissue, and is sensitive to cell density, axon size and possibly the thickness of the myelin sheath. Lack of myelin and decrease in cell density increases ADC, and this may explain the strong negative correlation between PSR and ADC. Moreover, as $R_{1obs}$ is inversely correlated with axon size which in turn is related to ADC, it follows that PSR will also be inversely related to ADC. FA values could be affected by axonal size and density, coherence of fibers, and myelination. A positive correlation is observed between FA and PSR suggesting that axonal damage is associated with demyelination. Correlation between PSR and FA was hardly apparent in previous studies of the brain (51,52). The presence of the high correlation in the cord could be a consequence of the much more ordered and unidirectional microstructure. In the brain, FA may be dominated by orientation dispersion. Given the findings we obtained in monkeys, qMT could become the first choice to reveal white matter microstructure and integrity of human spinal cord. The CEST measure of APT* is known to be sensitive to the presence of mobile proteins/peptides or the by-products of amino acids from degradation of macromolecules. The correlation between PSR and APT* is the weakest among the MRI parameters examined, confirming that APT* is strongly affected by the content of small metabolites and probably is not a measure of total protein or macromolecules. In summary, measures from different MRI methods including qMT are consistent with each other while providing unique information about the recovery process of the injured SC tissue including the injury-induced cyst.

### Interpretation of tissue properties using MRI parameters

MRI measures are indirect indicators of tissue pathology, so considerations of the signal source and possible contributors are critical for the interpretation of the findings. The AV at the onset is edema or cyst like, based on its unusually low cellular density, high composition of mobile metabolites and low macromolecular level. High or increased $T_{2a}$ values could be related to a considerable increase in the extracellular water space, which presumably expands due to demyelination or relates to gliosis. At the cyst, the large positive APT* at PP could be due to inflammation related increases in specific mobile metabolites, and/or the accumulation of the by-products of amino acids from neurotransmitters. The high values of $T_{1obs}$ and ADC at PP indicate low cellularity and less restricted water diffusion. The lower PSR of the cyst and the tissue around the cyst, and the later decrease after the appearance of cyst, are related to the unilateral demyelination and gliosis of local tissues around the cyst. PSR, $RM_{0b}$, $T_{1obs}$, $T_{2a}$, ADC and FA values of the cyst significantly differed from those of normal tissue at the end point (EP), indicating an incomplete cyst repair at 6 month after SCI. A complete return of APT* value to baseline indicated that the inflammation and secondary injury process likely ended. These observations underscore the importance of

multi-parametric MRI for the study of pathogenesis after SCI. More specific MRI quantification is more informative for assessing tissue properties and functions *in vivo*.

### Challenges in quantitative MRI of spinal cord in small animals at ultra-high field

The experiments described rely on the ability to robustly acquire high resolution, artifact free data from small structures in live animals. The use of high field increases the signal to noise and image quality but also there are significant potential sources of artifact. We selected pulsed MT for studying SCI because firstly, sequences with long TR are more sensitive to motion and CSF pulsation, and secondly, SAR is lowered using pulsed saturation. The variation of $B_1$ was less than 7% in the spinal cord (in 20 mm length), but larger than 10% close to the 2 ends of the coil. The RMS value of $\Delta B_0$ was ~60 Hz (in a $15\times25\times30$ $mm^3$ volume), but $\Delta B_0$ could be larger than 100 Hz for pixels close to the two ends of coil. The qMT measurements were restricted to the homogeneous region, because $B_1$ and $B_0$ corrections are inadequate in regions where the deviations from nominal values are extremely large. In this work, only the middle 1.5 cm section of the spinal cord was chosen for ROI analysis.

Even though high signal-to-noise ratios offered at high fields permit high resolution, partial volume averaging still may have impact on quantitative measurements because much higher resolution is required for small cords. Partial volume effects would be more pronounced in DTI measures in this study, because the diffusion-weighted EPI sequence is more sensitive to $B_0$ and motion. While our ROIs were selected based on MTC images in this study, the FA ($0.45\pm0.02$) of GM could be overestimated because the selected ROI was more affected by motion and partial volume effects.

## CONCLUSION

Our experimental results demonstrate that qMT measurements are robust and sensitive for detecting dynamic changes in tissue properties in regions rostral and caudal to injury. Extracting parameters from qMT reduces the influence of sequence variables, and is more specific for characterizing demyelination and levels of macromolecules. The combination of longitudinal *in vivo* qMT imaging with other MRI methods such as DTI and CEST will provide complementary information about the pathophysiological basis of the progression and recovery from the injury to the spinal cord.

## Supplementary Material

Refer to Web version on PubMed Central for supplementary material.

## ACKNOWLEDGEMENT

We thank Mr. Fuxue Xin and Mrs. Chaohui Tang of the Vanderbilt University Institute of Imaging Science for their assistance in MRI data collection and animal care. We also thank Dr. Hui-Xin Qi for her advice on tissue histology. This study is supported by a grant from Dana foundation to LMC and NIH grants NS069909-01 to LMC, NS078680-01 to JCG, CA184693 and EB017767 to DG.

## REFERENCES


1. Kaas JH, Qi HX, Burish MJ, Gharbawie OA, Onifer SM, Massey JM. Cortical and subcortical plasticity in the brains of humans, primates, and rats after damage to sensory afferents in the dorsal columns of the spinal cord. Exp Neurol. 2008; 209(2):407–416. [PubMed: 17692844]
2. Thuret S, Moon LD, Gage FH. Therapeutic interventions after spinal cord injury. Nat Rev Neurosci. 2006; 7(8):628–643. [PubMed: 16858391]
3. Jones TB, McDaniel EE, Popovich PG. Inflammatory-mediated injury and repair in the traumatically injured spinal cord. Curr Pharm Des. 2005; 11(10):1223–1236. [PubMed: 15853679]
4. Guest JD, Hiester ED, Bunge RP. Demyelination and Schwann cell responses adjacent to injury epicenter cavities following chronic human spinal cord injury. Exp Neurol. 2005; 192(2):384–393. [PubMed: 15755556]
5. Totoiu MO, Keirstead HS. Spinal cord injury is accompanied by chronic progressive demyelination. J Comp Neurol. 2005; 486(4):373–383. [PubMed: 15846782]
6. Silver J, Miller JH. Regeneration beyond the glial scar. Nat Rev Neurosci. 2004; 5(2):146–156. [PubMed: 14735117]
7. Fawcett JW. Overcoming inhibition in the damaged spinal cord. J Neurotrauma. 2006; 23(3-4):371–383. [PubMed: 16629623]
8. Smith SA, Edden RA, Farrell JA, Barker PB, Van Zijl PC. Measurement of T1 and T2 in the cervical spinal cord at 3 tesla. Magn Reson Med. 2008; 60(1):213–219. [PubMed: 18581383]
9. Smith SA, Golay X, Fatemi A, Mahmood A, Raymond GV, Moser HW, van Zijl PC, Stanisz GJ. Quantitative magnetization transfer characteristics of the human cervical spinal cord in vivo: application to adrenomyeloneuropathy. Magn Reson Med. 2009; 61(1):22–27. [PubMed: 19097204]
10. Ellington BM, Schmit BD, Gourab K, Sieber-Blum M, Hu YF, Schmainda KM. Diffusion heterogeneity tensor MRI (?-Dti): mathematics and initial applications in spinal cord regeneration after trauma - biomed 2009. Biomed Sci Instrum. 2009; 45:167–172. [PubMed: 19369758]
11. Fujiyoshi K, Yamada M, Nakamura M, Yamane J, Katoh H, Kitamura K, Kawai K, Okada S, Momoshima S, Toyama Y, Okano H. In vivo tracing of neural tracts in the intact and injured spinal cord of marmosets by diffusion tensor tractography. The Journal of neuroscience : the official journal of the Society for Neuroscience. 2007; 27(44):11991–11998. [PubMed: 17978040]
12. Wang F, Qi HX, Zu Z, Mishra A, Tang C, Gore JC, Chen LM. Multiparametric MRI reveals dynamic changes in molecular signatures of injured spinal cord in monkeys. Magn Reson Med. 2014 doi: 10.1002/mrm.25488.
13. Cohen AB, Neema M, Arora A, Dell'oglio E, Benedict RH, Tauhid S, Goldberg-Zimring D, Chavarro-Nieto C, Ceccarelli A, Klein JP, Stankiewicz JM, Houtchens MK, Buckle GJ, Alsop DC, Guttmann CR, Bakshi R. The relationships among MRI-defined spinal cord involvement, brain involvement, and disability in multiple sclerosis. J Neuroimaging. 2012; 22(2):122–128. [PubMed: 21447024]
14. Harel NY, Strittmatter SM. Functional MRI and other non-invasive imaging technologies: providing visual biomarkers for spinal cord structure and function after injury. Exp Neurol. 2008; 211(2):324–328. [PubMed: 18396280]
15. Agosta F, Filippi M. MRI of spinal cord in multiple sclerosis. J Neuroimaging. 2007; 17(Suppl 1): 46S–49S. [PubMed: 17425735]
16. Abe M, Komori H, Yamaura I, Kayano T. Spinal cord herniation into an extensive extradural meningeal cyst: postoperative analysis of intracystic flow by phase-contrast cine MRI. J Orthop Sci. 1999; 4(6):450–456. [PubMed: 10664429]
17. Ahmad I, Rosenbaum AE, Yu FS, Collins GH, Collins CS, Poe LB. Intrinsic cervical spinal cord deformation on MRI: “the distorted ‘H’ sign”. J Spinal Disord. 1996; 9(6):494–499. [PubMed: 8976489]
18. Ahn SJ, Kim IO. Spinal cord glioblastoma induced by radiation therapy of nasopharyngeal rhabdomyosarcoma with MRI findings: case report. Korean J Radiol. 2012; 13(5):652–657. [PubMed: 22977336]
19. Alblas CL, Bouvy WH, Lycklama ANGJ, Boiten J. Acute spinal-cord ischemia: evolution of MRI findings. J Clin Neurol. 2012; 8(3):218–223. [PubMed: 23091532]

20. Amster JL. MRI proves superiority in evaluating spinal cord. Diagn Imaging (San Franc). 1991; 13(8):76–82. [PubMed: 10149731]
21. Andreoli C, Colaiacomo MC, Rojas Beccaglia M, Di Biasi C, Casciani E, Gualdi G. MRI in the acute phase of spinal cord traumatic lesions: Relationship between MRI findings and neurological outcome. Radiol Med. 2005; 110(5-6):636–645. [PubMed: 16437049]
22. Appel B, Moens E, Lowenthal A. MRI of the spine and spinal cord: infectious and inflammatory pathology. J Neuroradiol. 1988; 15(4):325–334. [PubMed: 3252012]
23. Bejjani GK, Rizkallah RG, Tzortidis F, Mark AS. Cervical spinal cord injury during cerebral angiography with MRI confirmation: case report. Neuroradiology. 1998; 40(1):51–53. [PubMed: 9493190]
24. Beslow LA, Ichord RN, Zimmerman RA, Smith SE, Licht DJ. Role of diffusion MRI in diagnosis of spinal cord infarction in children. Neuropediatrics. 2008; 39(3):188–191. [PubMed: 18991201]
25. Bot JC, Barkhof F. Spinal-cord MRI in multiple sclerosis: conventional and nonconventional MR techniques. Neuroimaging Clin N Am. 2009; 19(1):81–99. [PubMed: 19064202]
26. Carsin M, Gandon Y, Rolland Y, Simon J. MRI of the spinal cord: intramedullary tumours. J Neuroradiol. 1987; 14(4):337–349. [PubMed: 3450798]
27. Ford JC, Hackney DB, Joseph PM, Phelan M, Alsop DC, Tabor SL, Hand CM, Markowitz RS, Black P. A method for in vivo high resolution MRI of rat spinal cord injury. Magn Reson Med. 1994; 31(2):218–223. [PubMed: 8133758]
28. Wheeler-Kingshott CA, Stroman PW, Schwab JM, Bacon M, Bosma R, Brooks J, Cadotte DW, Carlstedt T, Ciccarelli O, Cohen-Adad J, Curt A, Evangelou N, Fehlings MG, Filippi M, Kelley BJ, Kollias S, Mackay A, Porro CA, Smith S, Strittmatter SM, Summers P, Thompson AJ, Tracey I. The current state-of-the-art of spinal cord imaging: applications. Neuroimage. 2014; 84:1082–1093. [PubMed: 23859923]
29. Stroman PW, Wheeler-Kingshott C, Bacon M, Schwab JM, Bosma R, Brooks J, Cadotte D, Carlstedt T, Ciccarelli O, Cohen-Adad J, Curt A, Evangelou N, Fehlings MG, Filippi M, Kelley BJ, Kollias S, Mackay A, Porro CA, Smith S, Strittmatter SM, Summers P, Tracey I. The current state-of-the-art of spinal cord imaging: methods. Neuroimage. 2014; 84:1070–1081. [PubMed: 23685159]
30. Wolff SD, Eng J, Balaban RS. Magnetization transfer contrast: method for improving contrast in gradient-recalled-echo images. Radiology. 1991; 179(1):133–137. [PubMed: 2006263]
31. Wolff SD, Chesnick S, Frank JA, Lim KO, Balaban RS. Magnetization transfer contrast: MR imaging of the knee. Radiology. 1991; 179(3):623–628. [PubMed: 2027963]
32. Wolff SD, Balaban RS. Magnetization Transfer Contrast (Mtc) and Tissue Water Proton Relaxation In Vivo. Magnetic Resonance in Medicine. 1989; 10(1):135–144. [PubMed: 2547135]
33. Odrobina EE, Lam TY, Pun T, Midha R, Stanisz GJ. MR properties of excised neural tissue following experimentally induced demyelination. NMR Biomed. 2005; 18(5):277–284. [PubMed: 15948233]
34. Catalaa I, Grossman RI, Kolson DL, Udupa JK, Nyul LG, Wei L, Zhang X, Polansky M, Mannon LJ, McGowan JC. Multiple Sclerosis: Magnetization Transfer Histogram Analysis of Segmented Normal-appearing White Matter1. Radiology. 2000; 216(2):351–355. [PubMed: 10924552]
35. McDaniel JD, Ulmer JL, Prost RW, Franczak MB, Jaradeh S, Hamilton CA, Mark LP. Magnetization Transfer Imaging of Skeletal Muscle in Autosomal Recessive Limb Girdle Muscular Dystrophy. Journal of Computer Assisted Tomography. 1999; 23(4):609–614. [PubMed: 10433295]
36. Aisen AM, Doi K, Swanson SD. Detection of liver fibrosis with magnetic cross-relaxation. Magnetic Resonance in Medicine. 1994; 31(5):551–556. [PubMed: 8015410]
37. Quesson B, Bouzier AK, Thiaudiere E, Delalande C, Merle M, Canioni P. Magnetization transfer fast imaging of implanted glioma in the rat brain at 4.7 T: interpretation using a binary spin-bath model. Journal of Magnetic Resonance Imaging. 1997; 7(6):1076–1083. [PubMed: 9400852]
38. Ng MC, Hua J, Hu Y, Luk KD, Lam EY. Magnetization transfer (MT) asymmetry around the water resonance in human cervical spinal cord. J Magn Reson Imaging. 2009; 29(3):523–528. [PubMed: 19243033]

39. Liu H, Chen G, Zhang W, Zhu JY, Lin ZQ, Gong ZC, Wang FQ, Jia J, Sun ZJ, Zhao YF. Overexpression of macrophage migration inhibitory factor in adenoid cystic carcinoma: correlation with enhanced metastatic potential. J Cancer Res Clin. 2013; 139(2):287–295.
40. Henkelman RM, Huang XM, Xiang QS, Stanisz GJ, Swanson SD, Bronskill MJ. Quantitative Interpretation of Magnetization-Transfer. Magnetic Resonance in Medicine. 1993; 29(6):759–766. [PubMed: 8350718]
41. Sled JG, Pike GB. Quantitative interpretation of magnetization transfer in spoiled gradient echo MRI sequences. Journal of Magnetic Resonance. 2000; 145(1):24–36. [PubMed: 10873494]
42. Gochberg DF, Gore JC. Quantitative imaging of magnetization transfer using an inversion recovery sequence. Magnetic Resonance in Medicine. 2003; 49(3):501–505. [PubMed: 12594753]
43. Ramani A, Dalton C, Miller DH, Tofts PS, Barker GJ. Precise estimate of fundamental in-vivo MT parameters in human brain in clinically feasible times. Magn Reson Imaging. 2002; 20(10):721–731. [PubMed: 12591568]
44. Cercignani M, Barker GJ. A comparison between equations describing in vivo MT: the effects of noise and sequence parameters. Journal of Magnetic Resonance. 2008; 191(2):171–183. [PubMed: 18191599]
45. Cercignani M, Alexander DC. Optimal acquisition schemes for in vivo quantitative magnetization transfer MRI. Magn Reson Med. 2006; 56(4):803–810. [PubMed: 16902982]
46. Pluim JPW, Maintz JBA, Viergever MA. Mutual-information-based registration of medical images: A survey. Ieee T Med Imaging. 2003; 22(8):986–1004.
47. Qi HX, Chen LM, Kaas JH. Reorganization of somatosensory cortical areas 3b and 1 after unilateral section of dorsal columns of the spinal cord in squirrel monkeys. The Journal of neuroscience : the official journal of the Society for Neuroscience. 2011; 31(38):13662–13675. [PubMed: 21940457]
48. Chen LM, Qi HX, Kaas JH. Dynamic reorganization of digit representations in somatosensory cortex of nonhuman primates after spinal cord injury. The Journal of neuroscience : the official journal of the Society for Neuroscience. 2012; 32(42):14649–14663. [PubMed: 23077051]
49. Norenberg MD, Smith J, Marcillo A. The pathology of human spinal cord injury: Defining the problems. J Neurotrauma. 2004; 21(4):429–440. [PubMed: 15115592]
50. Janve VA, Zu Z, Yao SY, Li K, Zhang FL, Wilson KJ, Ou X, Does MD, Subramaniam S, Gochberg DF. The radial diffusivity and magnetization transfer pool size ratio are sensitive markers for demyelination in a rat model of type III multiple sclerosis (MS) lesions. Neuroimage. 2013; 74:298–305. [PubMed: 23481461]
51. Underhill HR, Yuan C, Yarnykh VL. Direct quantitative comparison between cross-relaxation imaging and diffusion tensor imaging of the human brain at 3.0 T. Neuroimage. 2009; 47(4):1568–1578. [PubMed: 19500678]
52. Ou X, Sun SW, Liang HF, Song SK, Gochberg DF. The MT pool size ratio and the DTI radial diffusivity may reflect the myelination in shiverer and control mice. NMR Biomed. 2009; 22(5): 480–487. [PubMed: 19123230]

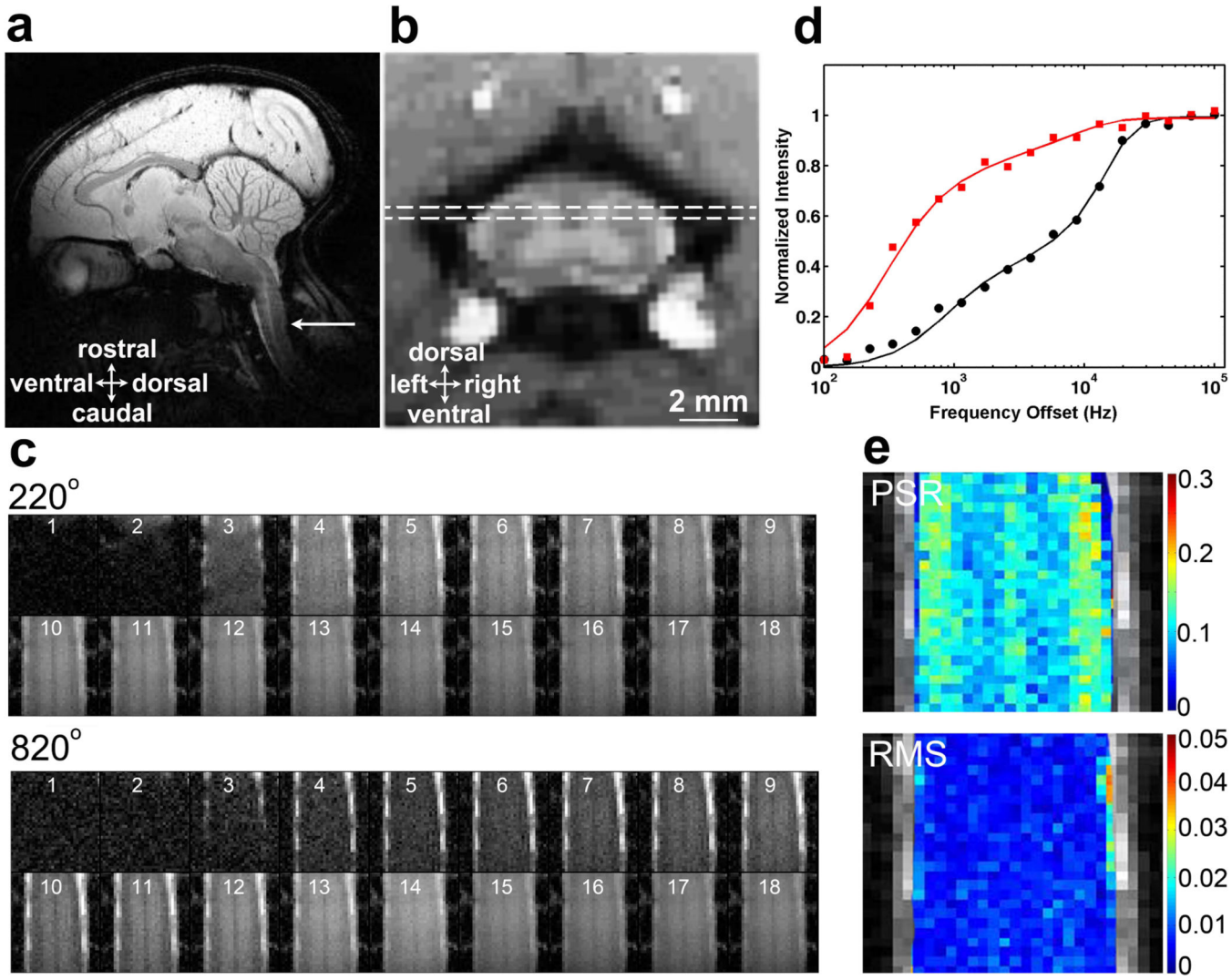


**Figure 1. QMT data acquisition and quantification**

(a) Sagittal view of a squirrel monkey brain. The white arrow indicates the location of the cervical spinal cord. (b) The dotted white line rectangle on an axial image shows the placement of the coronal slice that encompasses the region of a dorsal column lesion. (c) Raw qMT data cropped to be centered on the spinal cord. Images 1-18 are at 18 different RF offsets ranged between 100 Hz and 100 kHz with a constant logrithmic interval. (d) The fitting of the model to MT *in-vivo* data of regular gray matter at a selected pixel in spinal cord at two flip angles of $\theta_{sat}$ 820° (black circles) and 220° (red squares). Curves are normalized to maximum intensity. (e) Pool size ratio (PSR) map with color-coded values, and root mean squares of the residuals (RMS) from model fitting.

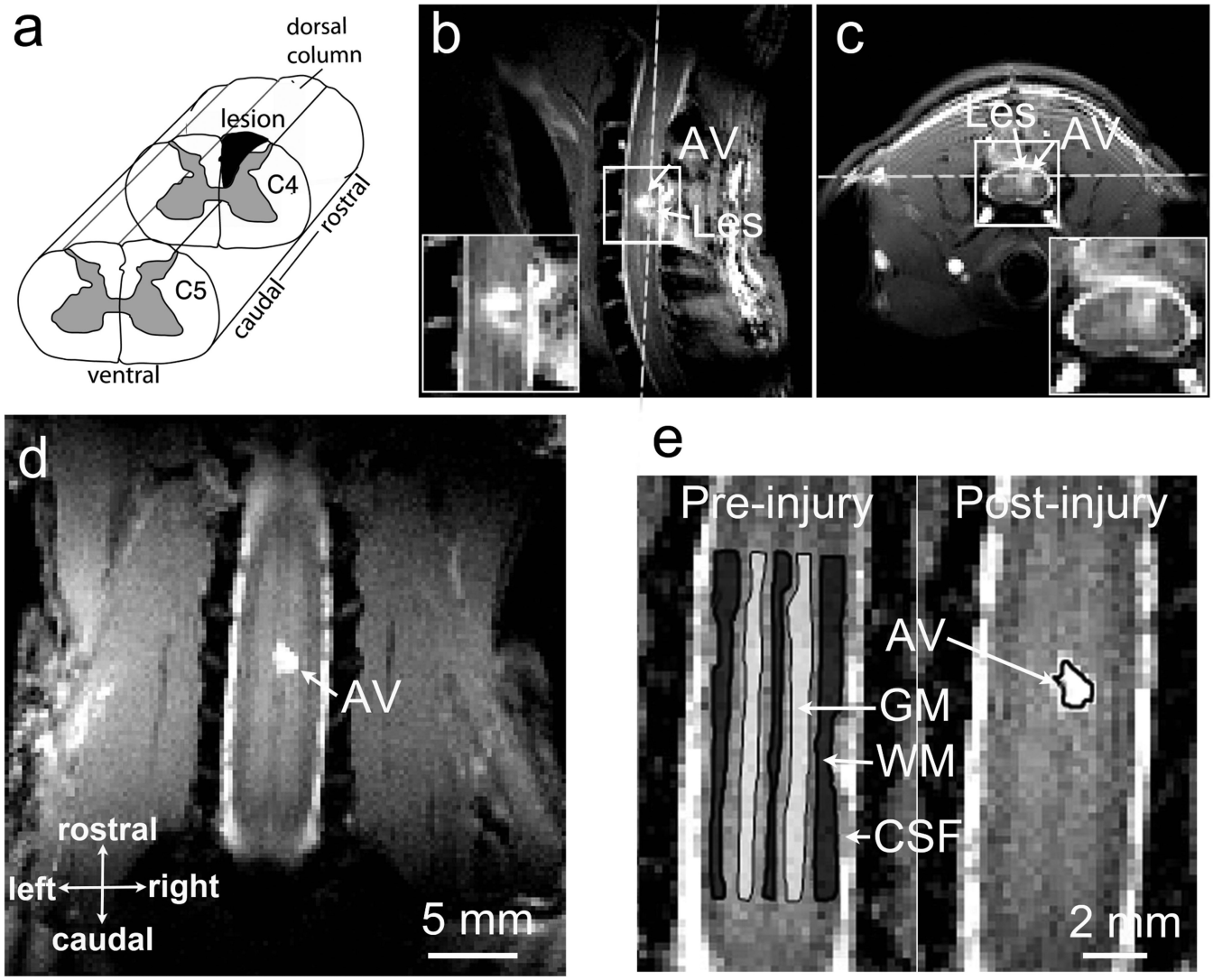


**Figure 2. Illustration of the spinal cord injury at C4 level in one representative squirrel monkey**

(a) Targeted unilateral lesion of the dorsal column. (b-c) Sagittal and axial MTC images obtained at 7 weeks post lesion. White dash lines show the position of a coronal image slice. (d) The coronal image used for qMT quantification. (e) Selections of ROIs for the regional statistical analysis. C4: cervical 4; WM: white matter; GM: gray matter; CSF: cerebrospinal fluid; AV: abnormal signal volume. AV was later determined to be cyst. SM-G shown.

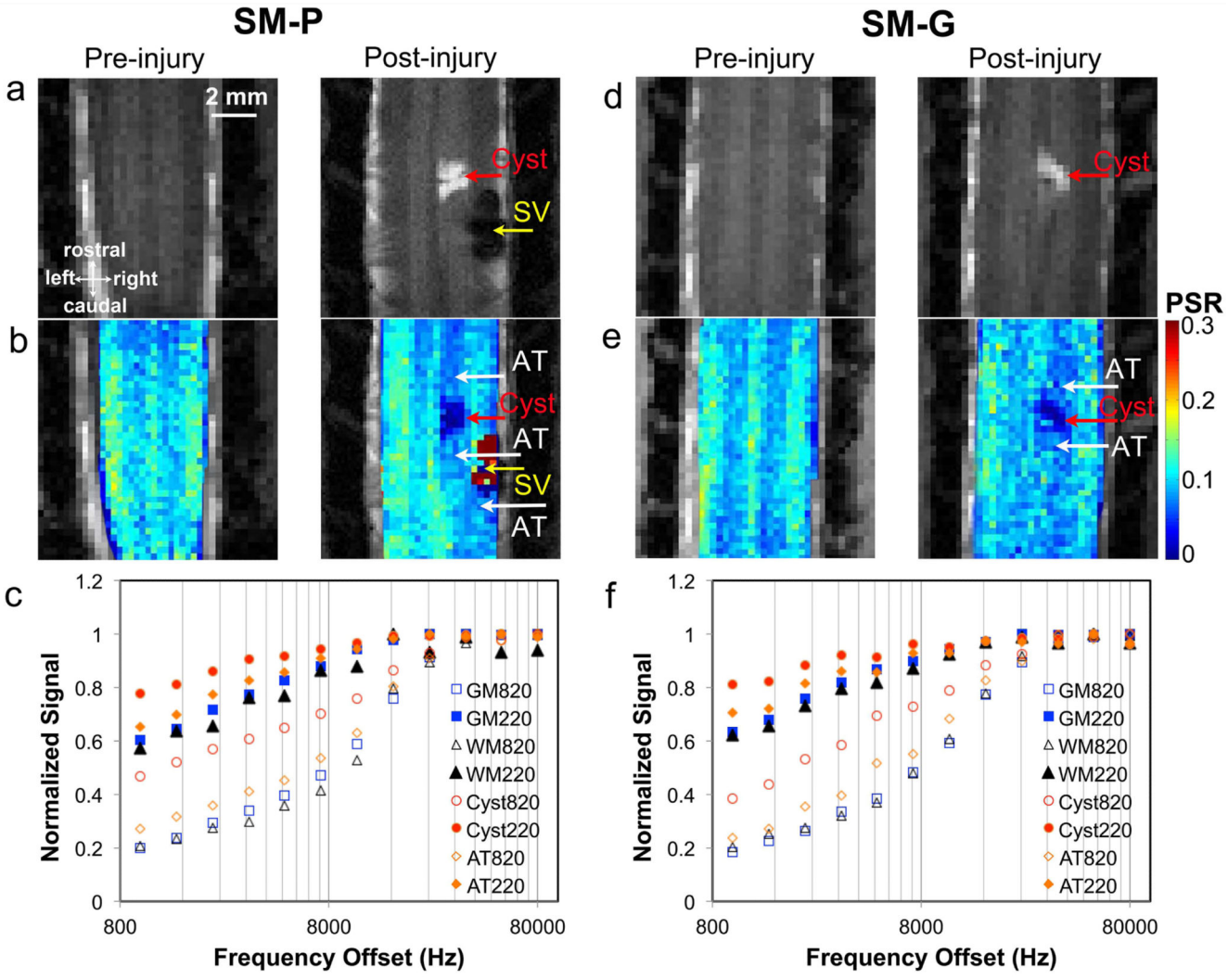


**Figure 3. Comparison of PSR maps and MT curves in pre- and post- injury conditions**

(a) & (d): Pre- and post- injury longitudinal MTC images showing the cyst (AV, abnormal volume) and a signal void (SV) caused by the lesion. (b) & (e): Pre- and post- injury PSR maps. AT, abnormal tissue with decreased PSR. The PSR of the SV region could not be determined due to the low intensity in the raw images. (c) & (f): MT spectra of normal WM and GM, cyst and AT obtained at different MT saturation flip angle 220° (solid markers) and 820° (open markers). Monkeys SM-P and SM-G shown.

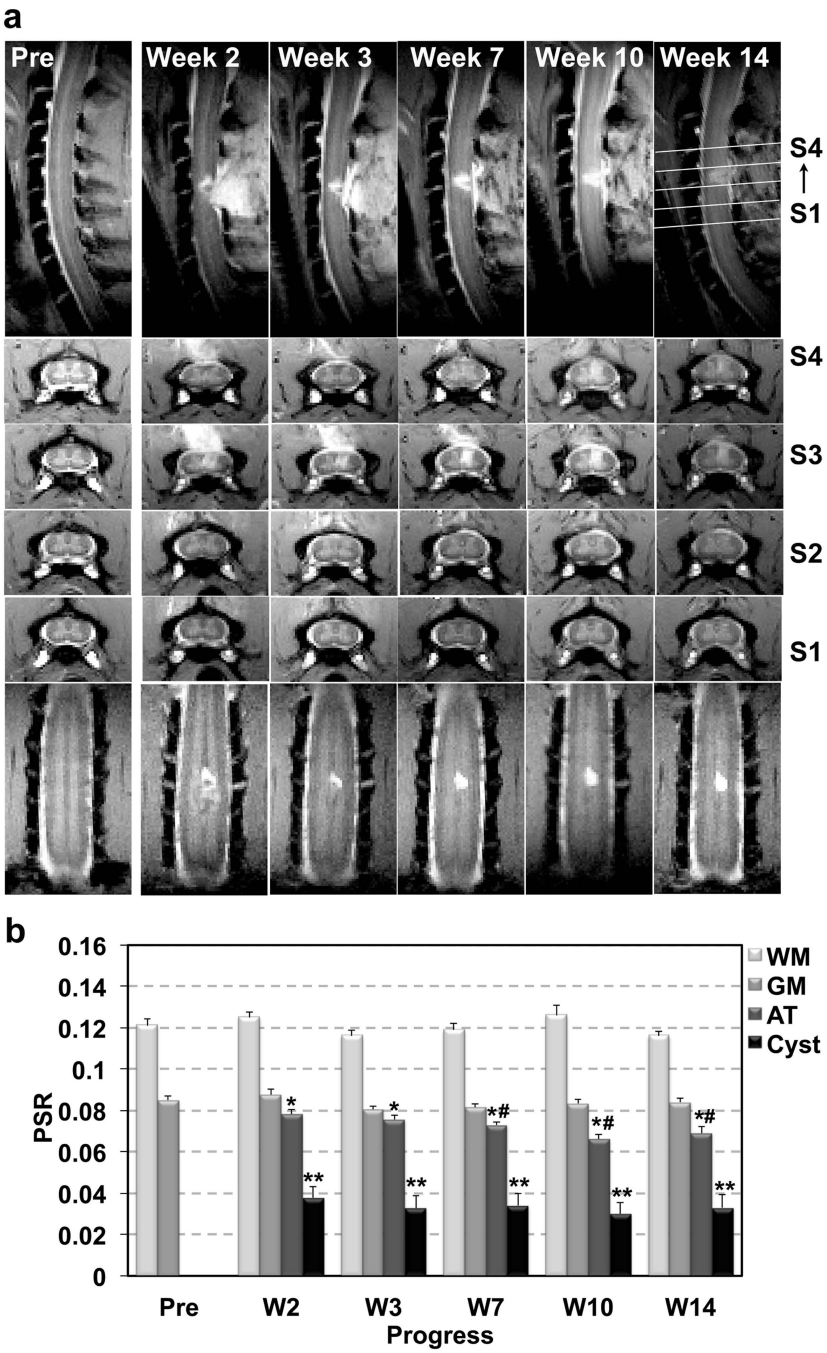


**Figure 4. Longitudinal assessments of lesion associated anatomical and PSR changes in one representative subject**

(a) Sagittal, axial and coronal MTC images showing the progression of the dorsal column lesion and lesion-related tissue property changes. (b) Mean PSR from different ROIs obtained before and at different time points after SCI. Error bars indicate standard errors calculated across voxels. SM-G shown. * $p < 0.05$ and ** $p < 0.01$ vs. control, and # $p < 0.05$ vs. abnormal tissue (AT) of post-lesion week 2.

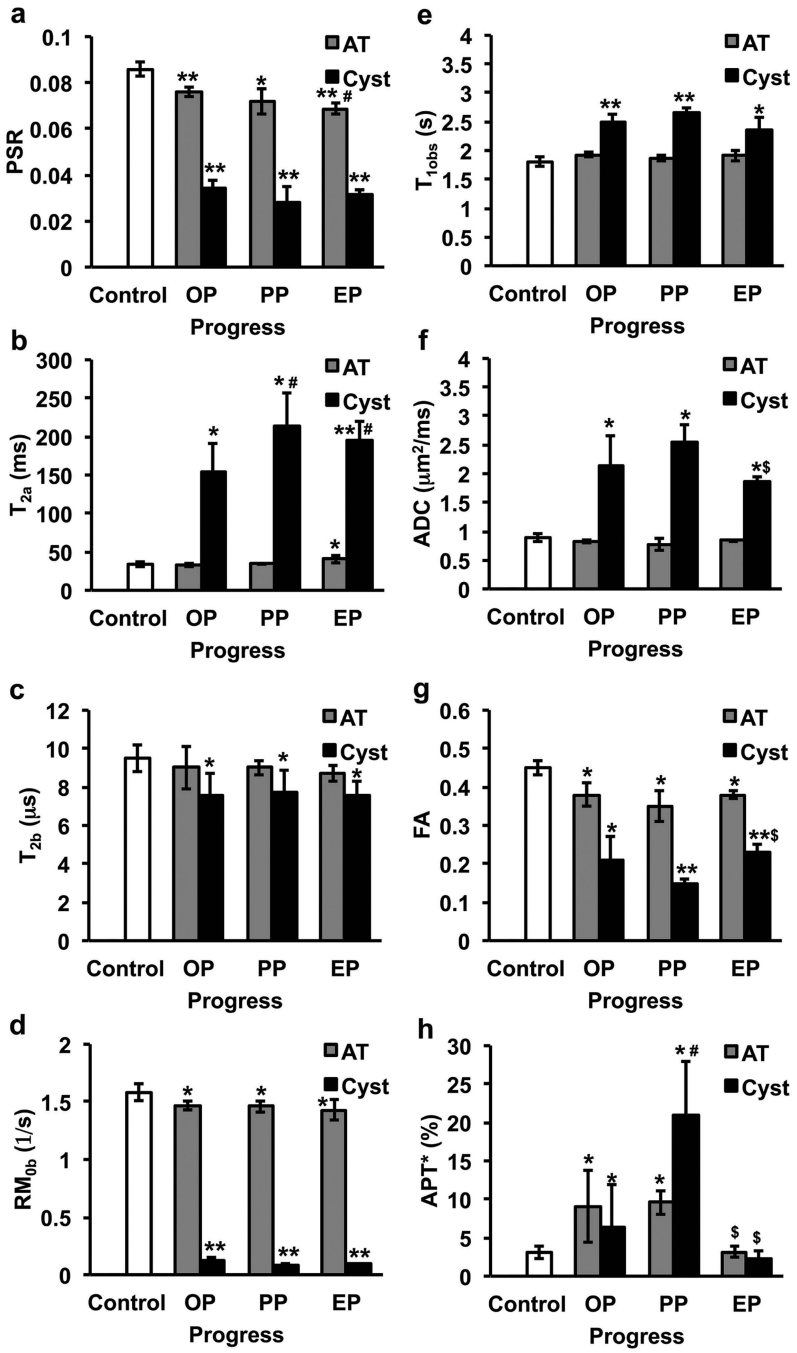


**Figure 5. Comparison of qMT and other MRI parameters of cyst and abnormal tissue at different stage after SCI**

(a) PSR, (b) $T_{2a}$, (c) $T_{2b}$, (d) $RM_{0b}$, (e) $T_{1obs}$, (f) ADC, (g) FA, and (h) APT*. The stage when cyst occurrence is defined as OP (onset point, 2 weeks after SCI), the stage when the APT* of cyst is maximum during the progress is defined as PP (peak point), and the stage the APT* of cyst is minimum is defined as EP (end point) since it is the end time point in the longitudinal study. N=9 for the control (regular GM), and N=3 for cyst and AT. Standard deviations are across subjects. * $p < 0.05$ and ** $p < 0.01$ vs. control, # $p < 0.05$ vs. relative onset value, and $ $p < 0.05$ vs. relative peak value. AT: abnormal tissue.

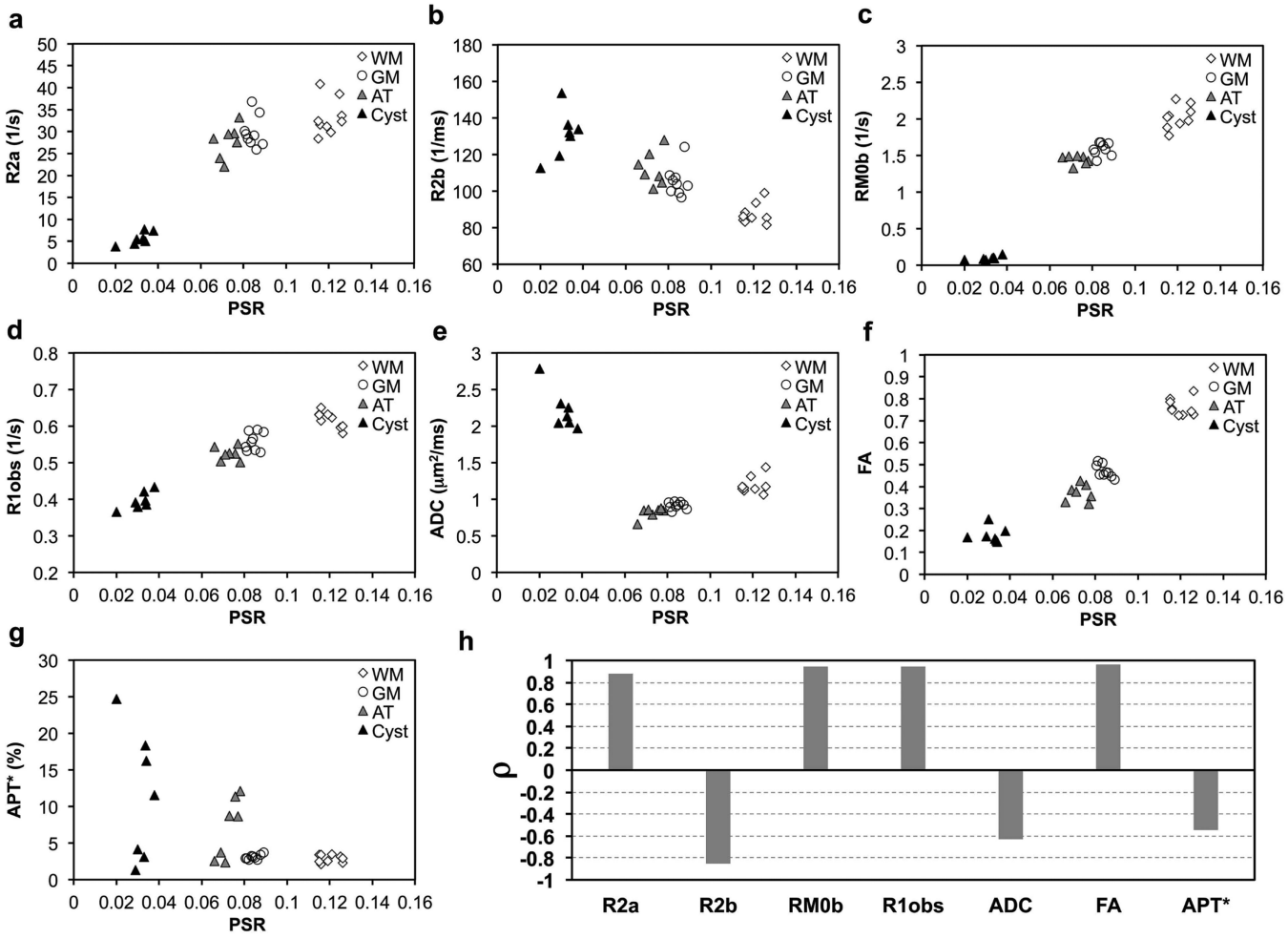


**Figure 6. Correlations between PSR and other MRI parameters**

(a)-(g) Plots of $R_{2a}$, $R_{2b}$, $RM_{0b}$, $R_{1obs}$, overall ADC, FA and APT* values as a function of PSR. (h) Comparison of regional Pearson correlation coefficients (ρ) between PSR and other parameters. WM: white matter; GM: gray matter; AT: abnormal tissue.

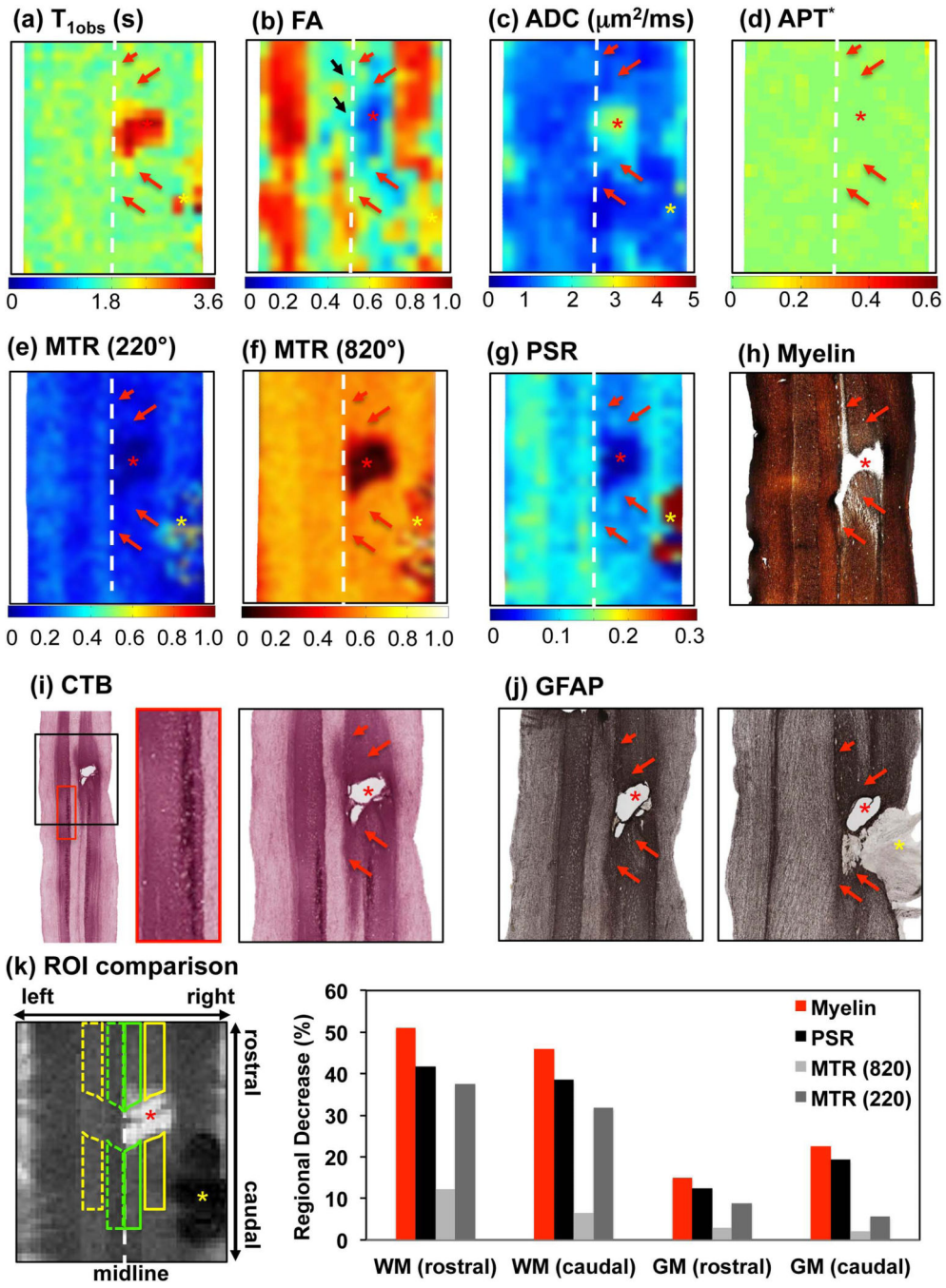


**Figure 7. Histological correlate of MRI maps in SM-P**

(a)-(d) Color-coded conventional $T_{1obs}$, FA, ADC and APT* maps. (e)-(g) Color-coded MTR (220°, RF offset at 5000 Hz), MTR (820°, RF offset at 5000 Hz), and PSR maps. Red asterisk indicates the cyst. Red arrows indicate the affected abnormal tissue (AT) regions at above and below cyst/lesion location. Yellow asterisk indicates the signal void (SV) region. (h)(i)(j) Corresponding spinal cord tissue with Myelin, CTB (Cholera Toxin B) and GFAP (Glial Fibrillary Acidic Protein) stains, respectively. The enlarged CTB in the red box indicates CTB labels. Yellow asterisk in GFAP indicates filling tissue, at the corresponding

lesion site. (k) Regional demyelination comparison around the lesion. Region of filling tissues was excluded from comparison due to the signal void in MRI data, which might be from hemorrhage (yellow asterisk in k). MRI data shown were for the end point (24 weeks after injury), and histologic sections were done 2 weeks later.

## Table 1

Comparison of the averaged regional qMT parameters

| Time | ROI | PSR | $T_{2a}$ (ms) | $T_{2b}$ (μs) | $RM_{0b}$ ($s^{-1}$) |
|---|---|---|---|---|---|
| Pre- | GM | 0.086 ± 0.003 | 33.9 ± 3.7 | 9.5 ± 0.7 | 1.58 ± 0.07 |
| | WM | 0.120 ± 0.005 | 30.5 ± 3.4 | 11.5 ± 0.7 | 2.02 ± 0.16 |
| Post- | GM | 0.084 ± 0.003 | 33.4 ± 4.0 | 9.4 ± 0.7 | 1.59 ± 0.09 |
| | WM | 0.116 ± 0.005 | 30.2 ± 3.7 | 11.6 ± 0.7 | 2.01 ± 0.16 |

Values are shown as Mean ± SD (standard deviation). The pre-lesion (Pre-) values were calculated across the mean of subjects in normal conditions (n=9). The post-lesion (Post-) values of normal GM and WM were obtained from the non-lesion side of the spinal cord across multiple sessions in three animals with SCI.